Effect of bioparticle size on dispersion and retention in monolithic and perfusive beds

Egor I. Trilisky[1], Abraham M. Lenhoff[*]

Department of Chemical Engineering, University of Delaware, Newark, DE 19716, USA

ABSTRACT

Single-component pulse response studies were used to compare the retention and transport behavior of small molecules, proteins, and a virus on commercially available monolithic and perfusive ion-exchangers. Temporal distortion and extra-column effects were corrected for using a simple algorithm based on the method of moments. It was found that temporal distortion is inversely related to the number of theoretical plates. With increasing bioparticle size, retention increased and the transition from a non-eluting to a non-adsorbing state with increasing ionic strength became more abrupt. Both of these observations are qualitatively explained by calculations of particle–surface electrostatic attractive energy. Calculations also suggest that, for sufficiently large bioparticles, such as viruses or cells, hydrodynamic drag can promote elution. Under non-adsorbing conditions, plate height increased only weakly with flow rate and the skew remained unchanged. With increasing retention, plate height increased dramatically for proteins. Plate height was scaled by permeability rather than bead diameter to enable comparison among different stationary phases.

© 2010 Elsevier B.V. All rights reserved.

1. Introduction

As the biotechnology industry matures, chromatography is being applied to purification of increasingly larger biologics, raising questions regarding size-dependent differences in the chromatographic behavior of bioparticles. Explicitly considering the size of a biologic as an independent variable can lead to a more thorough understanding of chromatography and can help select operating parameters suited for a biologic of a given size. Comparison of bioparticles of different sizes also differs from most chromatographic investigations, which are typically carried out with one particular biologic of interest or a few comparable ones. This work is particularly aimed at improving purification or removal of large bioparticles, such as viruses.

We examine the effect of analyte size by comparing the chromatographic behavior of small molecules, proteins, and a virus. In order to isolate particle size as the independent variable, the model bioparticles are all negatively charged at the conditions used and their surface charge densities are of the same order of magnitude, while the particle diameter spans two orders of magnitude. The model proteins have pI values similar to that of the model virus – adenovirus type 5 (Ad5), which is used extensively in gene therapy, including the two gene therapy drugs already approved in China [1,2]. Although small molecules were included mainly to span a broader range of probe sizes, pulses of small molecules, especially acetone and NaCl, are typically used to analyze the quality of column packing, so it is of interest to evaluate how good a model such small molecules are for proteins.

Selecting an appropriate stationary phase is one of the main challenges in chromatographic process development. Resins with small diffusive pores (10–100 nm) work very well for purification of most proteins. For larger biologics, diffusion is slow and transport may be enhanced by convection – the objective of perfusive resins [3–6] and monoliths [7–10], including membrane adsorbers [11–13]. Direct side-by-side comparisons among these different classes of adsorbents are rare [14–17]. Here we compare monolithic and perfusive stationary phases for a range of sizes of biologics along with making some theoretical predictions for a wider range of parameter combinations. Although membrane adsorbers can be

* Corresponding author. Tel.: +1 302 831 8989; fax: +1 302 831 1048.
E-mail address: lenhoff@udel.edu (A.M. Lenhoff).
[1] Current address: Amgen, 1201 Amgen Ct W, Seattle, WA 98119, USA.

very useful in applications that require binding dilute components, they were not included in these experiments because they cannot easily be compared directly to packed beds due to drastic differences in bed height.

The mode of chromatography chosen for the stationary phase comparison was anion-exchange, but many of the findings are likely to be applicable to other modes as well. The comparison was performed by single-component pulse response experiments under both adsorbing and non-adsorbing conditions. Pulse response studies provide information on porosity, retention, band broadening and skew. A comparison of porosities, binding capacities, and permeabilities was presented previously [17]; here we address differences in retention behavior and peak shape.

Retention in adsorptive chromatography of small molecules and most proteins is determined by a balance between the interaction of the adsorbate with the stationary phase and the thermal motion of the adsorbate, which opposes binding. For larger adsorbates, hydrodynamic drag can also contribute to bioparticle elution in adsorbents that allow significant convection near the adsorbent surface. The drag force has been examined extensively for rolling of cells on flat surfaces [18–20], but it has not been taken into account in studies of chromatographic systems. Several reports indicate that shear forces can be critical for achieving cell desorption or preventing cells from binding [21–23]. If the drag force on adsorbate particles is comparable to or greater than the force of attraction, retention could be reduced at higher flow rates. Additionally, drag could limit dynamic binding capacity by preventing larger bioparticles from binding in parts of a stationary phase where convection is high. It was previously shown that drag can result in flow-dependent entrapment of virus particles in chromatography columns [24]. Here we discuss other deviations from typical chromatographic behavior that can result from drag and present equations that can be used to determine whether drag is important in a given system.

As for peak shape, the main figures of merit usually considered in characterizing chromatographic transport are the height equivalent to a theoretical plate (H) and peak asymmetry (As). These measures are important not only for analytical columns, but also for preparative ones because a poorly packed column can have a decreased dynamic binding capacity in addition to lower resolution. Besides the packed bed itself, the extra-column flow path can distort and broaden a peak [25]. A less obvious cause for peak skew occurs regardless of packed bed quality – temporal distortion skews a peak because the detector is in a fixed position and a peak is monitored in time and not in space [26]. The peak appears skewed because the tail has a longer residence time than the front, so the tail spreads further. Observed peak parameters, particularly skew or asymmetry, can differ significantly from their true (spatial) values.

In most cases, this relativity problem has been either overlooked or considered negligible, despite having been known for decades. The issue has been addressed most explicitly by Jönsson [27] and Pai [26], who provided expressions for the detector output corresponding to a peak that is Gaussian on the column, although errors appear in some of the equations in [27]. The effects of extra-column dispersion are accounted for in some cases, using the additivity of the moments [28,29]. In this work we revisit the effect of temporal distortion and present a simple practical method to estimate both temporal distortion and extra-column effects. We derive corrective functions for temporal moments of a spatially Gaussian peak and propose that applying these functions can indicate whether temporal distortion has a significant impact on a given parameter or trend.

The approach taken addresses both of the most commonly used methods for peak analysis, namely the method of moments (MoM) [30] and the method referred to here as the "classic" method, which assumes a Gaussian peak and uses the time at peak maximum as the elution time (t_R), the width at half height (w_h) to calculate the number of theoretical plates (N), and signal values at 10% of peak height to obtain the peak asymmetry (As). These and other less common methods for measuring column efficiency have been summarized previously [31]. Of the manual methods, the 3–5 σ techniques can be more accurate than the classic method discussed here, but they still assume a Gaussian peak, so they are inherently less accurate than the MoM, which makes no assumptions. One limitation of the MoM, however, is that, with increasing moment number, the sensitivity to noise increases.

Fortunately, only the first two moments are needed to calculate N. The third moment is required to find *skew*, which is an alternative to As. In general, N is a more important parameter than As or *skew* because it determines resolution and pool concentration. For a sufficiently narrow peak, *skew* and As are irrelevant. As was introduced in the classic method to identify situations where a peak is narrow in the middle (large N), but has appreciable tailing or fronting. However, the MoM makes the use of As or *skew* largely unnecessary. Despite the ready availability of computers to perform rigorous peak analysis, the classic method continues to be widely used, and most commercially available software packages do not generally offer the MoM as an alternative; an exception is Dionex's Chromeleon software. In addition to accounting for temporal distortion and extra-column effects, this work compares the two peak analysis methods to aid column qualification and development of peak analysis software.

2. Theory

2.1. Empirical equation for a chromatographic peak

The calculations of band broadening used to estimate the extent of temporal distortion are based on the equilibrium-dispersive model of chromatography [32]. In this ideal model, the analyte pulse spreads by a Fickian dispersion process as it migrates along the column at a constant migration velocity u; the dispersion mechanisms are not considered explicitly, but their combined magnitude is characterized by a constant axial dispersion coefficient, D_{ax}. The resulting peak is spatially Gaussian. The migration velocity u is that of the center of mass of the peak, regardless of retention or lack thereof. In dimensionless form, the resulting differential equation is

$$\frac{\partial \rho}{\partial \tau} + \frac{\partial \rho}{\partial Z} = \frac{1}{Pe^*}\frac{\partial^2 \rho}{\partial Z^2}, \tag{1}$$

where ρ is the dimensionless concentration of the species being tracked, normalized such that the peak area is 1, Z is the dimensionless axial position in the column, normalized by the column length L, Pe^* is the Péclet number, and τ is the dimensionless time:

$$Pe^* \equiv \frac{Lu}{D_{ax}} \quad \text{and} \quad \tau \equiv \frac{ut}{L}. \tag{2}$$

The input pulse can usually be approximated as a Dirac delta function at the origin initially, at time $t = 0$, a distance L (bed height) away from a fixed-point detector.

In an infinite domain, boundary conditions at the column ends are neglected, and the solution to Eq. (1) is

$$\rho = \sqrt{\frac{Pe^*}{4\pi\tau}}\exp\left[-Pe^*\frac{(Z-\tau)^2}{4\tau}\right]. \tag{3}$$

It has been shown that the choice of axial boundary conditions has little effect in modeling of chromatographic systems at sufficiently high Péclet numbers [32,33]. Eq. (3) describes the distribution of molecules in a pulse as a function of both time and axial position. The main point of interest is when/where the detection
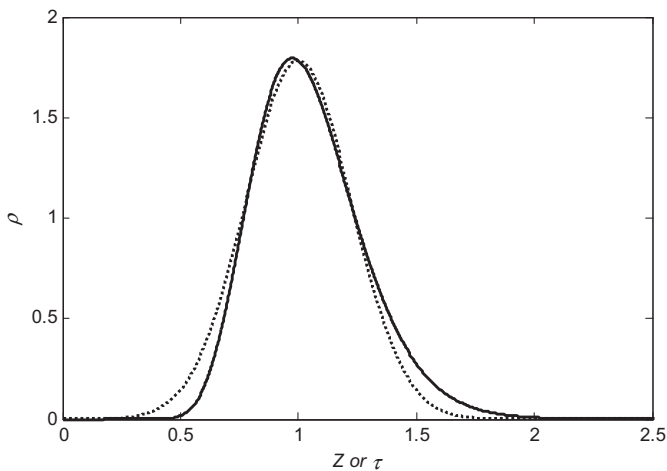
Fig. 1. A Gaussian band ($\cdots$) appears skewed (—) when detected in time at the outlet of a chromatography column. Arbitrary $Pe = 40$.

occurs: either at $\tau = 1$ if the whole peak is viewed at once when its maximum reaches the detector or at $Z = 1$ if the peak is observed in time by a fixed-point detector, which is generally the case in chromatography. Fig. 1 shows an example of a spatially Gaussian peak and its skewing by temporal distortion; both were generated using Eq. (3).

2.2. Peak parameters from the method of moments (MoM)

It follows from Eq. (3) that temporal distortion does not change the peak area in this case: the temporal ($Z = 1$) and spatial ($\tau = 1$) zeroth moments are

$$m_{0T} = \int_0^\infty \rho \, d\tau = 1 \quad \text{and} \quad m_{0S} = \int_{-\infty}^\infty \rho \, dZ = 1. \tag{4}$$

Although temporal distortion does not affect the peak area for the spatially Gaussian peak given by Eq. (3), the area can be affected in other cases. As an example, consider case A1 in [34], where an initially sharp band starts off at the origin and is carried through a circular tube by laminar flow. The band is distorted only by the parabolic velocity profile (diffusion is neglected), resulting in a rectangular distribution of the area-average concentration, one end of which remains at the origin. In this case, the signal trace recorded by the fixed-position detector, i.e., the observed (temporal) peak, is inversely proportional to time. Integrating this peak to infinite time gives infinite area, whereas the spatial area at any given time is a finite constant. In most practical cases, the area is not expected to change greatly, but temporal distortion may affect mass balances that are based on peak areas if the peak deviates significantly from Gaussian. In this work, the peak area is assumed to remain constant.

Since moments higher than m_0 are generally normalized by the peak area [30], such normalization is used here as well. The conversion between temporal and spatial moments requires a factor of u^i, but here we use dimensionless moments: the ith temporal moment is normalized by t_R^i and the ith spatial moment by L^i. This simplifies the results in that all parameters of interest and the corresponding corrective functions depend on Pe^* (Eq. (2)) as the sole parameter. The temporal (m_{1T}) and spatial (m_{1S}) first moments for Eq. (3) are

$$m_{1T} = \int_0^\infty \tau \rho \, d\tau = 1 + \frac{2}{Pe^*} \quad \text{and} \quad m_{1S} = \int_{-\infty}^\infty Z \rho \, dZ = 1. \tag{5}$$

Table 1
Moments for a spatially Gaussian peak passing through a fixed-point detector and the corresponding corrective functions needed to account for temporal distortion.

Moment	Spatial	Temporal	Corrective function
m_0	1	1	No correction
m_1	1	$1 + \frac{2}{Pe^*}$	$m_{1T}^* = \frac{m_{1T}}{1 + 2/Pe^*}$
m_2'	$\frac{2}{Pe^*}$	$\frac{2}{Pe^*}\left(1 + \frac{4}{Pe^*}\right)$	$m_{2T}'^* = \frac{m_{2T}'}{1 + 4/Pe^*}$
m_3'	0	$\frac{12}{Pe^{*2}} + \frac{64}{Pe^{*3}}$	$m_{3T}'^* = m_{3T}' - \frac{12}{Pe^{*2}} - \frac{64}{Pe^{*3}}$
m_4'	$\frac{12}{Pe^{*2}}$	$\frac{12}{Pe^{*2}}\left(1 + \frac{18}{Pe^*} + \frac{80}{Pe^{*2}}\right)$	$m_{4T}'^* = \frac{m_{4T}'}{1 + (18/Pe^*) + (80/Pe^{*2})}$

We use Eq. (5) to correct the first temporal moment for temporal distortion by introducing a corrective function:

$$m_{1T}^* = \frac{m_{1T}}{1 + 2/Pe^*}. \tag{6}$$

Variables corrected for temporal distortion are indicated by asterisks. Central moments are used beyond the first moment to make analysis of peak shape symmetrical by effectively moving the peak to the origin. The ith central temporal and spatial moments (m_{iT}' and m_{iS}', respectively) are defined as

$$m_{iT}' = \int_0^\infty (\tau - m_{1T})^i \rho \, d\tau \quad \text{and} \quad m_{iS}' = \int_{-\infty}^\infty (Z - m_{1S})^i \rho \, dZ. \tag{7}$$

Results for moments 0–4 are summarized in Table 1. Moments higher than the second are not very useful in practice, but the third and fourth moments are included here for completeness to allow comparison to previous work [27].

The approach used here to correct for temporal distortion is based on estimating the apparent value of Pe^* from the temporal plate number, N_T. Since N is defined as [35]

$$N = \frac{m_1^2}{m_2'}, \tag{8}$$

where m_1 is the first moment and m_2' is the second central moment, the temporal and spatial N are

$$N_T = \frac{m_{1T}^2}{m_{2T}'} = \frac{(Pe^* + 2)^2}{2Pe^* + 8} \quad \text{and} \quad N_S = \frac{Pe^*}{2} = \frac{1}{m_{2S}'}, \tag{9}$$

and Pe^* can be obtained explicitly from N_T (the observed N) as

$$Pe^* = N_T - 2 + \sqrt{N_T^2 + 4N_T}. \tag{10}$$

Once Pe^* is calculated, the corrective functions in Table 1 can be employed.

Skew and excess (kurtosis) are defined as

$$skew = \frac{m_3'}{m_2'^{3/2}} \quad \text{and} \quad excess = \frac{m_4'}{m_2'^2} - 3. \tag{11}$$

Like other variables in this article, they can be either spatial or temporal. For a spatially Gaussian peak, the spatial skew and excess are both 0 and the temporal values are

$$skew = \frac{12Pe^* + 64}{(2Pe^* + 8)^{3/2}} \quad \text{and} \quad excess = \frac{3(Pe^* + 8)(Pe^* + 10)}{(Pe^* + 4)^2} - 3. \tag{12}$$

Additivity of the first three moments [28] allows accounting for extra-column effects by subtracting the moments of a no-column control from the corresponding moments with the column in the flow path. The correction for extra-column effects should be applied after the correction for temporal distortion. The corrected N and skew (if needed) can then be calculated using the corrected moments.

2.3. Peak parameters from the classic method

The classic method of finding N is based on the width of a peak at half of its height (w_h) and the assumption that the temporal peak is Gaussian. Peak asymmetry (As) is defined as the ratio of the backward and forward abscissa segments between the peak maximum and 10% of the peak maximum. Using Eqs. (3) and (8), we can derive the classic formula for spatial N of the Gaussian peak [36]:

$$N = 8\ln 2\left(\frac{\tau_{\max}}{w_h}\right)^2 \approx 5.55\left(\frac{\tau_{\max}}{w_h}\right)^2, \tag{13}$$

where τ_{max} is the observed time at peak maximum. For skewed peaks, Eq. (13) can significantly overestimate N. Also, accounting for extra-column dispersion requires analysis of no-column control peaks and dispersion peaks in relatively short open tubes are intrinsically non-Gaussian [34,37].

The corresponding analysis for the temporal case gives:

$$f^2 \frac{\tau_f}{\tau_{\max}} = \exp\left[\frac{Pe^*}{2}\left(\frac{(1-\tau_{\max})^2}{\tau_{\max}} - \frac{(1-\tau_f)^2}{\tau_f}\right)\right], \tag{14}$$

where $0 < f < 1$ is a fraction of peak height and τ_f is a set of two τ values at that value of f. A closed-form solution for τ_f could not be found. Taking the difference between numerical solutions for the two values of τ_f at $f = 0.5$ yields w_h. Substituting the numerical solution for w_h into Eq. (13) gives the classic N, which is plotted in Fig. 2A along with the observed N from the MoM and the spatial N from Eq. (9). To find As at 10% peak height ($f = 0.1$), Eq. (14) was solved numerically, but As also empirically correlates to:

$$As \approx \exp\left[\frac{(26N^2 + 7)^{0.747}}{5.2N^2 + 0.28N - 0.226}\right], \tag{15}$$

where the constants can be found by a least-squares fit to $\ln(As)$ [36].

2.4. Estimating drag force on adsorbed bioparticles

An order-of-magnitude estimate for the drag force (F_d) can be found from Stokes' Law:

$$F_d = 3\pi\mu u d_b, \tag{16}$$

where μ is the solution viscosity, u is the flow velocity around the particle, and d_b is the diameter of an adsorbed spherical bioparticle; this relation is approximate because it actually applies to freely suspended particles. Since flow is generally laminar in liquid chromatography, the average mobile-phase velocity around the particle adsorbed in a convective pore (u) can be estimated by assuming a steady parabolic velocity profile between two infinite plates separated by a distance equal to the pore diameter (d_p) [38]:

$$\frac{u(y)\varepsilon}{u_s} = 6(y - y^2), \tag{17}$$

where y is the normal distance from the surface, scaled by d_p, ε is the bed porosity, and u_s is the superficial flow velocity (u_s/ε is the average flow velocity). The average flow velocity around the adsorbed particle can be approximated by the velocity at a distance from the wall equal to that of the center of an adsorbed particle:

$$u\left(\frac{d_b}{2d_p}\right) = \frac{3d_b u_s}{d_p \varepsilon}\left(1 - \frac{d_b}{2d_p}\right), \tag{18}$$

If desired, d_b/d_p can be defined as a single variable. For the order-of-magnitude estimate here, the distribution of pore sizes is not taken into account.

In order to assess the importance of drag on adsorption, the relative magnitudes of drag and thermal forces in driving desorption

Table 2
Model probes and their characteristics.

Probe	Molecular weight	Hydrodynamic diameter (nm)	pI
NaCl (Na⁺, Cl⁻)	(23, 35)	(0.72, 0.66)	n/a
UMP	324	1.3	n/a
Ovalbumin	44,300	6	4.6
BSA	66,430	7	4.7
Ad5	170,000,000	100	4.5

are considered by calculating the ratio of the two effects (Φ) for a monolithic porous medium using Eqs. (16) and (18):

$$\Phi \equiv \frac{F_d d_b}{kT} = \frac{9\pi\mu u_s d_b^3}{d_p \varepsilon kT}\left(1 - \frac{d_b}{2d_p}\right). \tag{19}$$

If the pore diameter significantly exceeds the bioparticle diameter, Eq. (19) simplifies to

$$\Phi \approx \frac{9\pi\mu u_s d_b^3}{d_p \varepsilon kT}. \tag{20}$$

Eq. (19) or (20) can be used for monolithic porous media, including membranes or filters.

For binding of viruses and other large bioparticles onto typical packed beds, it is more accurate to use the interbead porosity, ε_i (typically 0.35–0.42 for spherical beads [39,40]) instead of the total porosity ε and the pore diameter between the resin beads, not within them, because virus particles bind on the outside and there is no significant flow through the resin beads. The d_p can then be estimated as $\varepsilon_i d_r$, where d_r is the diameter of the resin bead. Eq. (20) can be rewritten to find an order-of-magnitude estimate for the ratio of the drag and thermal forces for beds packed with spherical beads:

$$\Phi \approx \frac{200\mu u_s d_b^3}{d_r kT}. \tag{21}$$

For small viruses, such as MMV or AAV, Eqs. (20) and (21) indicate that the effect of drag should be significant in most moliths and in some filters, but not in packed beds. For larger viruses, such as XMuLV, Ad5, or HIV, the equations indicate that Φ can be of order 1 or larger even in packed beds, which suggests that virus binding can be affected by the drag at higher flow rates. Lower flow rates are recommended for improved virus binding in typical (non-perfusive) packed beds. Experimentally, drag effects can be separated from the effects of diffusion/binding kinetics by fixing the residence time and changing the bed dimensions and flow rate – drag depends only on the flow rate and not on the residence time.

It was previously shown that under non-binding conditions in monoliths, perfusive resins, and possibly filters, higher flow rates are more likely to trap viruses [24]. Comparing Eq. (20) to Eq. (4) in [24] (the Péclet number for the entrapment phenomenon, Pe') reveals that $\Phi \approx 3Pe'$. Since Φ and Pe' are both order-of-magnitude estimates, the point at which drag becomes important essentially coincides with the onset of convective entrapment if the appropriate constrictions are present.

3. Materials and methods

3.1. Model analytes

The model bioparticles for this work are listed in Table 2. The model small molecule uridine 5′-monophosphate (UMP, Sigma–Aldrich, St. Louis, MO, USA, cat # U6375, lot 32H0433) has a charge of −2 at pH 7.8, which was the pH used throughout. For the virus and the proteins, the hydrodynamic diameter given in Table 2 was measured by dynamic light scattering, as in [41], for
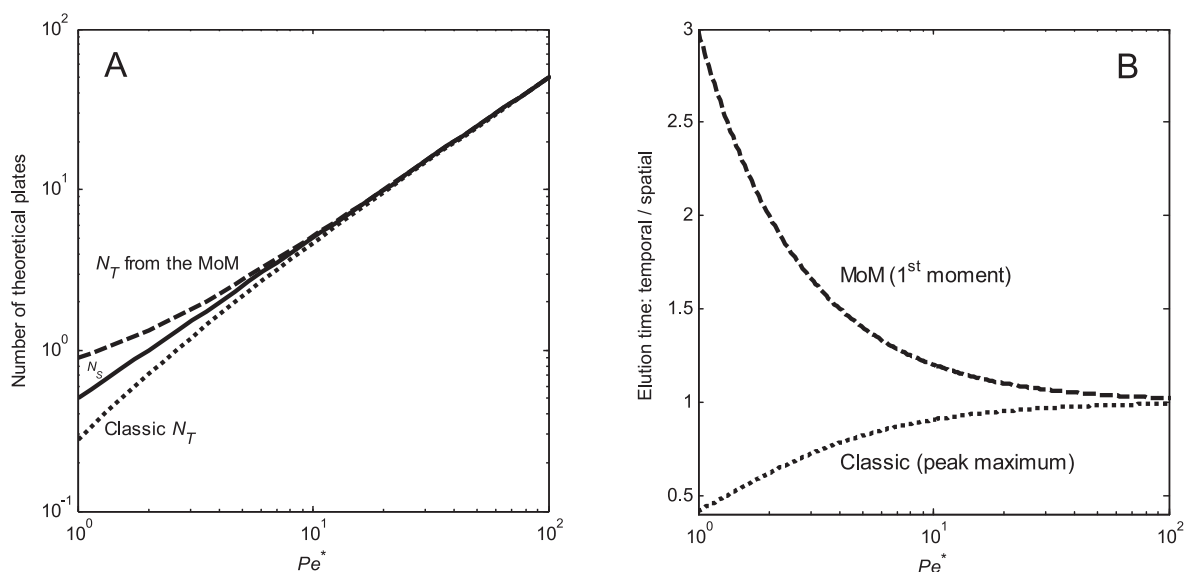
Fig. 2. Effects of temporal distortion on peak parameters of a spatially Gaussian peak. Dashed curves are from MoM and dotted ones are from the classic method.

UMP the diameter was estimated from the molecular structure, and for Na^+ and Cl^- the given diameters are those of hydrated ions [42]. As indicated in Table 2, the model proteins have pI values that are comparable to that of the model virus. The surface charge densities of UMP, the proteins, and Ad5 are estimated to have the same order of magnitude.

The net charge on the different proteins was found from the primary sequence and the average surface charge density was estimated by dividing the net charge by the solvent-accessible surface area, as previously reported [43]. The surface charge density on UMP was found by dividing the net charge on the molecule by the surface area of a sphere with the diameter of the molecule (approximately 1.3 nm). At the conditions used in these experiments (pH 7.8) the surface charge density is estimated to be roughly 60 mC/m² for UMP, 14 mC/m² for ovalbumin (Sigma–Aldrich, cat # A5503, lot 076K7045), 18 mC/m² for bovine serum albumin (BSA, Sigma–Aldrich, cat # A0281, lot 075K7545), and, for Ad5 (Baylor College of Medicine/Vector Development Lab, Houston, TX, USA, cat # Ad5-CMV-eGFP, lots 102307, 030206), between 9 mC/m² (value in [41], based on zeta potential measurements) and 88 mC/m² (calculated from charge values for the surface proteins of the virus, given in [44]). The discrepancy for Ad5 could be due either to binding of buffer components to the virus, which reduces its effective charge density, or to the presence of other charged components in the virus.

3.2. Stationary phases

Table 3 lists properties of the four stationary phases used in this study, three commercially available polymeric monoliths and a perfusive resin. The permeability and equivalent bead diameter values (K and d_e, respectively) in Table 3 were reported previously [17]. Monoliths were supplied with their own housings and the resin was packed into Waters AP-Minicolumns (0.5 cm i.d., $L = 4.8$ cm). The column was packed by resuspending the resin, pouring the slurry into the column/packing adaptor, letting the resin settle by gravity, flow packing at 4 mL/min (twice the maximum flow rate used in the experiments), and lowering the top to avoid any head space during the experiments. The bead size distribution for PL-SAX 4000 Å 10 μm was found using light microscopy [36,41]. The average bead diameter and the standard deviation by number, external surface area, and volume for this resin were determined to be

10.4 ± 2.8, 11.5 ± 1.8, and 11.8 ± 1.7 μm, respectively. The average intrabead pore diameter of this resin is 0.4 μm, according to the manufacturer.

3.3. Mobile phase

All experiments were performed under isocratic elution conditions in 20 mM HEPES (Sigma–Aldrich, cat # H4034) buffer, pH 7.8, with different NaCl (Fisher Scientific, Pittsburgh, PA, USA, cat # S271) concentrations to adjust the ionic strength. Buffers for work with Ad5 also contained 1.7% glycerol to avoid viscous fingering [45] because the stock Ad5 included glycerol. Attempts to dialyze the virus in dialysis cassettes failed because of binding of the virus particles to the cassette and the consequent low yield. Virus binding to containers has also been reported previously to reduce the yield over time [41]. Exchanging the buffer was not critical because the presence of small amounts of glycerol is not expected to interfere with the chromatography [46]. A pulse was assumed to be non-adsorbing if the ionic strength (I) was high enough that the peak elution time did not change with I. The salt concentrations used were 1.5 M NaCl for the virus and 1 M NaCl for the proteins and UMP.

3.4. Equipment

All chromatographic experiments were performed on an ÄKTA Explorer 100 (GE Healthcare, Uppsala, Sweden) with several modifications made to minimize the extra-column volume: flow direction and column selection valves were bypassed; the column inlet was connected to the injection valve using 20 cm of 0.25 mm ID tubing and the column outlet was connected to either the UV detector or the conductivity meter (in the case of NaCl pulse studies) using 58 cm of 0.25 mm ID tubing. These modifications reduced the extra-column volume to 5% of column volume or less. To account for extra-column effects (Section 2.2), control experiments without a column in place were performed. Ad5 and UMP were detected at 260 nm and proteins at 280 nm. The UV-900 detector was set to acquire data at the fastest available rate of every 0.1 s with the smallest available averaging time of 0.01 s. The C-900 conductivity meter refreshes the data sample every 1 s (fastest available rate). Data were exported from the Unicorn 5.01 software (GE Healthcare) in time mode instead of volume mode in order to allow more

Table 3
Characteristics of the stationary phases investigated.

Stationary phase	Manufacturer	Lot #	Bed dimensions (cm)		K (μm²)	d_e (μm)	Type	Base matrix	Functional group
			Diameter	Height					
DEAE CIM disks	BIA Separations (Ljubljana, Slovenia)	05-GE01-012-001B	1.2	0.3/disk	0.0063	3.1	Monolithic	Poly-methacrylate	Tertiary amine (DEAE)
ProSwift WAX-1S	Dionex (Sunnyvale, CA, USA)	006-06-012	0.46	4.4	0.026	6.1	Monolithic	Poly-methacrylate	Tertiary amine (DEAE)
UNO Q-1	Bio-Rad (Hercules, CA, USA)	Q1-4188	0.7	3.5	0.022	5.7	Monolithic	Poly-(acrylamide/vinyl)	Quaternary amine (Q)
PL-SAX 4000 Å 10 μm	Varian (Palo Alto, CA, USA)	10M-SAX 40-199A	0.5	4.8	0.093	11.8	Perfusive	PS-DVB	Quaternary amine (Q)

accurate time-to-volume conversion than in the Unicorn software. Subsequent peak analysis was performed using Matlab.

3.5. Pulse-response measurements and data analysis

A 30 μL sample loop was slowly filled by injecting 100 μL of a solution containing a model probe in order to minimize sample dilution due to non-plug flow during filling. After column equilibration and the start of sample injection, the injection valve was left in the inject mode for the remainder of the run to ensure that the entire sample entered the column. Analyte concentrations were approximately 3.5×10^{11} p/mL (0.1 g/L) for Ad5, 2.5 g/L for proteins, and 0.25 g/L for UMP. In the case of NaCl, 1 M NaCl pulses were run with a 0.15 M NaCl background. For retention studies, the superficial linear flow rate (u_s) was 1 cm/min. The flow rate was varied for unretained pulses. No-column controls were performed by using empty housing for CIM (zero bed height) and by completely bypassing the column for ProSwift, UNO and PL-SAX.

Peaks were analyzed using the method of moments [30] and corrected for extra-column effects and temporal distortion as described in Section 2.2. The retention factor k' was calculated from

$$k' = \frac{V_R - V_0}{V_0}, \tag{22}$$

where V_R and V_0 are the elution volumes under retentive and non-retentive conditions, respectively, both after subtracting the extra-column volume.

Band broadening was quantified in terms of the plate height, H, as described in the literature [30]. For a fair comparison among the different stationary phases, a reduced plate height (h) was defined based on the column permeability K as

$$h \equiv \frac{H}{38\sqrt{K}}, \tag{23}$$

where the constant in the denominator was introduced to make the results equivalent to those obtained using the traditional normalization of H by the resin bead diameter [47,48]. The constant was obtained by calculating the equivalent resin bead diameter (d_e) based on the hydraulic permeability, as has been done previously [49]. Using the Kozeny–Carman equation,

$$d_e = \sqrt{\frac{150(1 - \varepsilon_i)^2}{\varepsilon_i^3} K} = 38\sqrt{K}, \tag{24}$$

for a typical interstitial porosity in a packed bed ($\varepsilon_i = 0.35$). For the PL-SAX resin, d_e was calculated to be 11.8 μm, which is essentially the same as the measured average bead diameter for this resin.

Normalizing H by $\sqrt{K}$ not only allows comparison among all stationary phase types, but is also arguably a better way to compare conventional resins than using the bead diameter because the pressure drop is affected not only by the bead diameter, but also by resin compressibility, packing arrangement, and bead size distribution. The flow velocity was also scaled in terms of the corresponding Péclet number (Pe) as

$$Pe \equiv \frac{u_s d_e}{\varepsilon D} = \frac{38 u_s \sqrt{K}}{\varepsilon D}, \tag{25}$$

where D is the diffusivity of the analyte.

4. Results and discussion

4.1. Comparison of peak analysis methods

Fig. 2 compares N and elution time from the classic method and the MoM. Spatial elution time in this case (spatially Gaussian peak) is the time at which peak maximum exits the column. As expected, for large N (high Pe^*), the differences become negligible, as does the effect of temporal distortion. At small N, however, temporal distortion is significant. Extra-column effects can be accounted for by using no-column controls (zero bed height or column bypass), which have low N values and are therefore very susceptible to temporal distortion. Low N values are also expected for short bed heights and could even reach single digits in membrane chromatography [29]. Since the peak attributes can be parameterized in terms of only Pe^*, they can be expressed in terms of each other; Fig. 3 shows the dependence of As and $skew$ on N. Since As and $skew$ increase with decreasing N, lower bed heights are expected to lead to more asymmetric peaks. Also, the $skew$ trend in Fig. 3 suggests that Grushka's empirical observation that $skew$ generally varies as $L^{-1/2}$ [35] could be due to temporal shifting.

Column qualification typically involves ensuring that H and As fall within certain empirical limits that are generally based on values of H and As observed historically for other columns. The ideal (Gaussian) As value is typically taken to be 1, but for the observed As the ideal value is actually greater than 1 due to temporal distortion (Fig. 3). Fig. 3 can be used in column packing analysis to determine the "ideal" As instead of assuming that it is 1. Although Fig. 3 and Eq. (15) use N from the MoM, in the main range of interest ($N > 10$) they can also be used for the classic N since the two methods give essentially the same N in that range [36].

The first row of Table 4 compares uncorrected data from the classic method and the MoM using 383 actual runs. The data show that the results from the two methods tend to diverge as the moment number increases. The peak area (m_0) is found in the same way for the two methods. The classic elution time is fairly close to m_1. N, which is calculated from m_2, is significantly overestimated using the classic method because most of these peaks were skewed. The correlation between As and $skew$, both of which are found from m_3,

Table 4

Comparison of results obtained under non-interacting conditions for 383 runs using the bioparticles and stationary phases in Tables 2 and 3. The average values $\pm$ one standard deviation are given. Corrections to the MoM for extra-column effects (e-c.e.) and temporal distortion (t.d.) are included as indicated.

Compared properties and methods	t_R/m_1 or m_1/m_1	N/N	As – skew or skew – skew
Classic method vs. uncorrected MoM	0.93 ± 0.04	4.4 ± 2.9	0.6 ± 1.5
MoM: uncorrected vs. corrected for e-c.e. only	1.15 ± 0.08	0.80 ± 0.41	(1.4 ± 29)[a]
MoM: uncorrected vs. corrected for t.d. only	1.02 ± 0.02	1.001 ± 0.002	0.28 ± 0.10
MoM: uncorrected vs. corrected for both e-c.e. and t.d.	1.13 ± 0.07	0.96 ± 0.17	−0.4 ± 1.4

[a] Of the 383 skew values corrected for extra-column effects only (but not for temporal distortion), 12 were imaginary because the corresponding $m_2 \leq 0$; these data points were excluded from this value.

is even worse. As expected, when $As > 1$, *skew* is mainly positive, but there is no further correlation.

The last three rows of Table 4 examine the effects of extra-column contributions and temporal distortion in the MoM. Correction for both effects requires correcting the no-column control runs, which are significantly affected by temporal distortion due to their low N values. For m_1, extra-column effects were significant and temporal distortion had a relatively small effect. For N, the extra-column effects and temporal distortion of the no-column controls were important. When correction for extra-column effects was made without first correcting for temporal distortion, the m_2 was negative in 12 of 383 cases, which led to imaginary *skew* values. Correcting for temporal distortion eliminated this problem.

For the purposes of flow injection analysis of chromatographic beds, we recommend using the MoM and only m_0, m_1, and m_2. If the MoM is used, calculation of asymmetry or skew is not as important as in the classic method, as indicated by the fact that the classic N in Table 4 significantly exceeds the properly calculated N from the MoM (the average *skew* was 2.2, with a standard deviation of 1.2). In addition to the diminished importance of the peak skew in the MoM as compared to asymmetry in the classic method, it is best to avoid the use of skew whenever possible because m_3 is sensitive to noise. Extra-column effects and temporal distortion should be taken into account, however.

The correction for temporal distortion used here is exact only for spatially Gaussian peaks described by Eq. (3) – it is approximate for real peaks. If the evolution of a pulse in space-time in some system can be described more accurately by an expression different from Eq. (3), derivations analogous to Section 2.2 for corrective functions can be made. In the absence of such information,
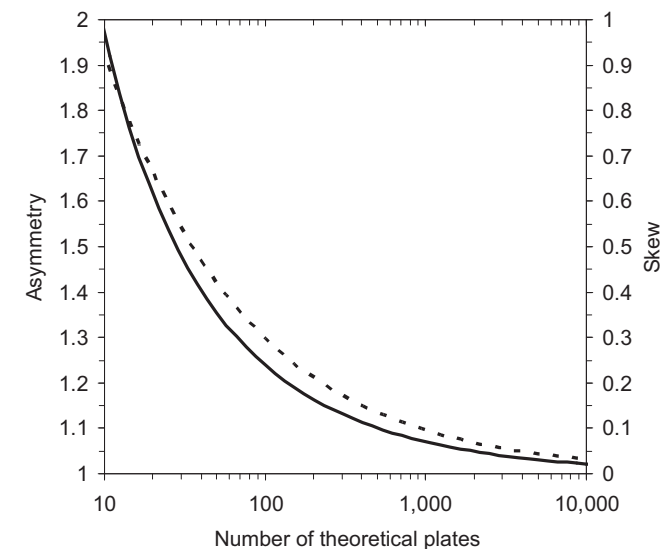
the algorithm in Section 2.2 and Table 1 can be used for typical chromatographic peaks. The correction can at least show whether temporal distortion is important for a given trend of interest.

4.2. Retention behavior

4.2.1. Effects of ionic strength

The general trend in retention with increasing probe size as a function of I is shown in Fig. 4 for the CIM disks. For the small molecule, there is a clear gradual shift of the elution peak to longer

Fig. 3. Dependence of calculated temporal asymmetry at 10% of peak height (solid line) and skew (dashed line) on temporal (observed) N for a spatially Gaussian peak. The N used here is from MoM.
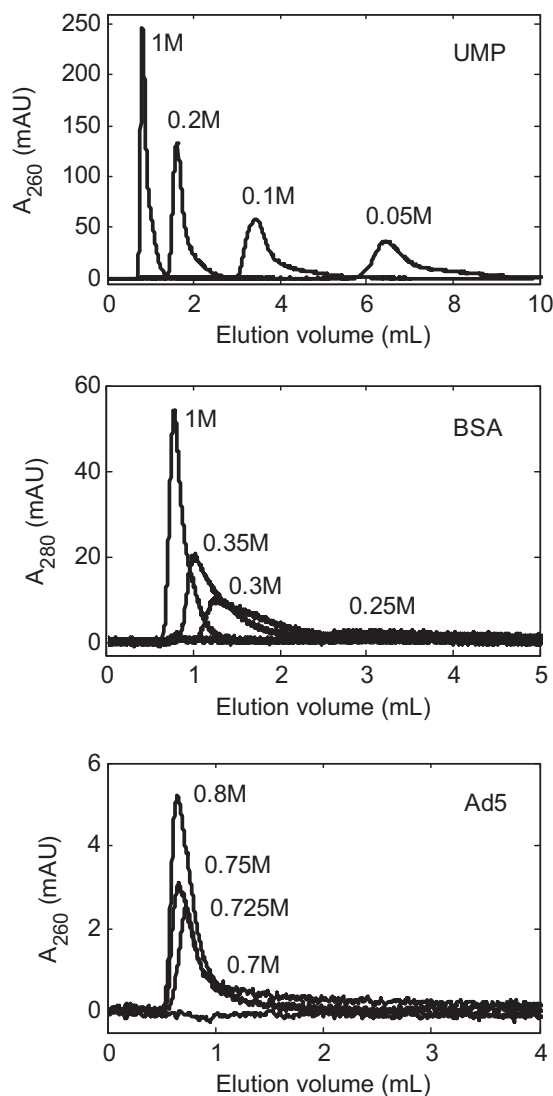

Fig. 4. Isocratic retention behavior for small molecule (top), protein (middle) and virus (bottom) at indicated ionic strengths; u_s = 1 cm/min; stationary phase: 4 DEAE CIM disks.
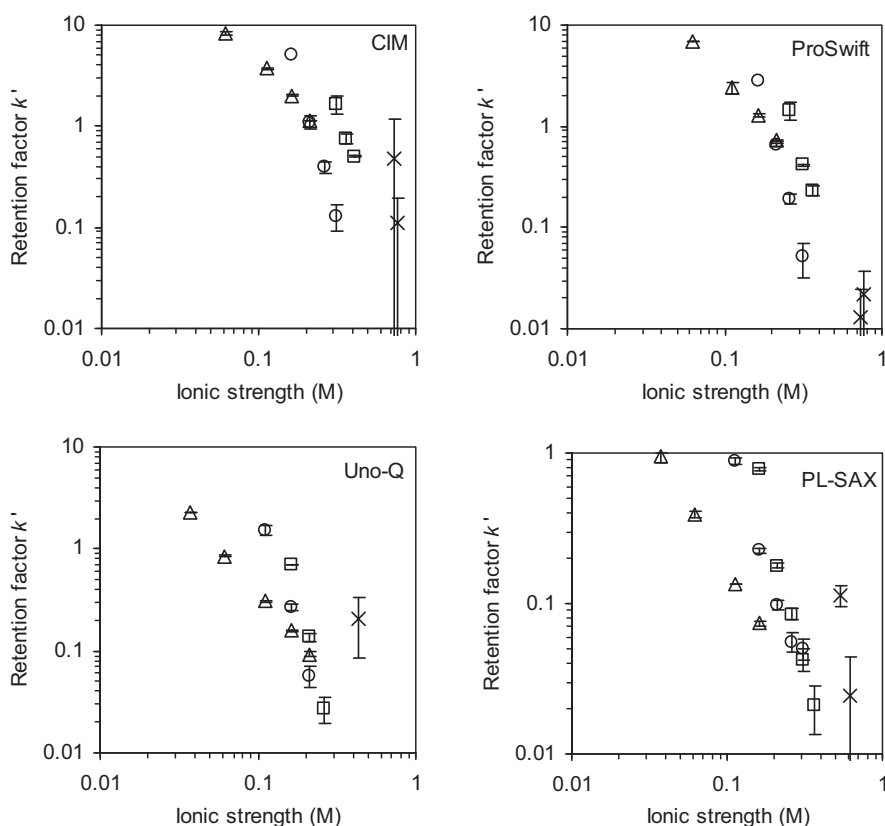
Fig. 5. Dependence of retention on ionic strength for UMP ($\triangle$), ovalbumin ($\bigcirc$), BSA ($\square$), and Ad5 ($\times$) on the four stationary phases. Correction for temporal distortion does not significantly impact these trends. Error bars indicate one standard deviation ($n = 2$–3); $u_s = 1$ cm/min.

retention times as I decreases. The shift also occurs for the protein, but over a narrower range of I and with increased band broadening. For the virus, there is almost no shift at all – as I decreases, it abruptly changes from a non-adsorbing to a non-eluting state. A practical implication of this phenomenon is that larger bioparticles can be loaded at higher I and elution can be performed with a relatively small step in salt concentration.

It is known that, in general, the range of I over which a protein can elute while still exhibiting finite retention is narrow and that higher I values are necessary to elute bioparticles that are more highly charged [50,51]. This is apparent when raw data such as those in Fig. 4 are expressed in dimensionless form in terms of k'. As expected [52], the $\log(k')$ vs. $\log(I)$ plots in Fig. 5 are linear. As the particle size increases, the lines shift to higher I and become steeper. The negative slopes of the lines, sometimes referred to as the characteristic charge on the bioparticle (Z_p) [52], were 1.6–1.8 for UMP on the four stationary phases, and 2.9–5.3 and 4.4–5.6, respectively, for ovalbumin and BSA.

All else being equal, larger bioparticles tend to have higher Z_p values. The small number of data points and large error bars on the Ad5 data in Fig. 5 are due to the steepness of the k' lines for Ad5 – the transition from a non-eluting to a non-interacting state is almost a step function of I for Ad5. Retention is comparable on the CIM and ProSwift monoliths, but is weaker on PL-SAX and substantially weaker on the Uno Q monolith. The general trends, however, are the same on all four stationary phases and correcting these data for temporal distortion did not affect these trends.

The trends are in agreement with qualitative predictions that can be made from calculations of the electrostatic interaction energy between a charged particle and an oppositely charged surface using colloidal principles [53–57], under the assumption that the surface charge density of the bioparticles remains constant with

increasing bioparticle size. A convenient measure of the electrostatic interaction energy between the adsorbate and the surface can be obtained from the Yukawa form for the particle–surface interaction energy, namely the interaction energy at contact (B_{ps}), defined as negative if attractive [55]. The dependence of B_{ps} on I can be estimated from the bioparticle and adsorbent surface charge densities, assuming that they are the sole determinants of the properties of the respective surfaces [54,57]. Fig. 6 shows that the magnitude of B_{ps} increases with particle size, so larger particles are more strongly attracted to the surface. Not surprisingly,
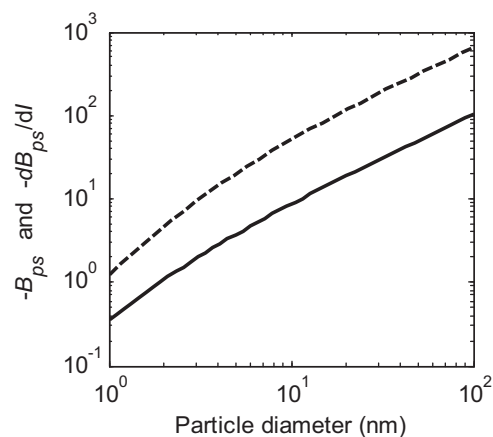

Fig. 6. Electrostatic attraction energy (scaled by kT, solid line) between a charged particle and an oppositely charged surface and the derivative of this energy with respect to ionic strength in units of mol/L (dashed line). Surface charge densities are 10 and 100 mC/m^2 for bioparticle and stationary phase, respectively. Ionic strength is 0.1 M.

therefore, the k' curves in Fig. 6 shift to higher I with increasing particle size. Additionally, Fig. 6 shows that the dependence of B_{ps} on I also increases with particle size, which is a plausible explanation for the steeper k' curves observed in Fig. 5 for larger bioparticles.

4.2.2. Predicted effects of drag

B_{ps} provides a measure of the particle–surface attraction relative to the thermal energy kT. In addition to the thermal motion, hydrodynamic drag could also contribute to bioparticle elution for larger adsorbates and thus reduce k' values in adsorbents that allow significant convection near the adsorbent surface. Fig. 7 shows an example of the thermal energy and the product of the drag force and the characteristic length scale, i.e., the radius of the adsorbate, relative to the energy of attraction between the adsorbate and the adsorbent. The model was developed to capture the qualitative trends and order-of-magnitude estimates, so it is only approximate. The parameters given in the figure caption are typical conditions that can be encountered in chromatography. For other specific conditions, the curves can be recalculated using Eq. (19) along with equations for B_{ps} [54–57]. For reference, surface charge densities have been reported to be around $9\,mC/m^2$ for Ad5 [41], 14–$44\,mC/m^2$ for proteins [58], and 66–$630\,mC/m^2$ for ion-exchangers [59].

Fig. 7 shows that, while the relative effect of the thermal force ($1/B_{ps}$) decreases with increasing particle diameter, the relative effect of drag increases, which suggests that very large bioparticles, such as cells, may elute because the drag contributes to desorbing them from the surface. Larger bioparticles would elute at lower I than would be expected from just electrostatic considerations. With increasing I, the electrostatic particle–surface attraction weakens and the relative effect of the drag and thermal forces
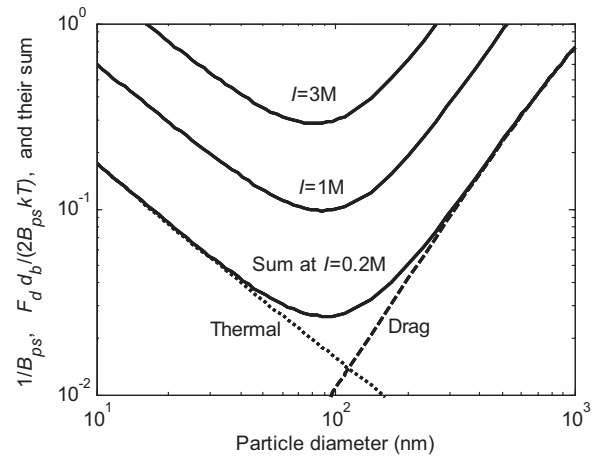

Fig. 7. Drag (– – –) and thermal (· · ·) energies, each normalized by the characteristic electrostatic energy of attraction between particle and surface; the sum of the drag and thermal energies (—) is shown at different I. Parameters used in this example: pore diameter = $1.5\,\mu m$, porosity = 0.55, $u_s = 1\,cm/min$, surface charge density = $10\,mC/m^2$ for the adsorbed particle and $100\,mC/m^2$ for the stationary phase.

increases, as indicated by the upward shift of the sum of the drag and thermal contributions with increasing I. The particle diameter at which the minimum occurs changes little with I, however.

Arvidsson et al. reported elution of *Escherichia coli* cells from an ion-exchange column at a fairly moderate 0.35–0.4 M NaCl [60]. The pore diameter in their monolith was in the range 10–100 μm, $\varepsilon > 0.9$, $u_s = 0.8\,cm/min$, and the size of *E. coli* is about 1–3 μm. Substituting these values into Eq. (19) shows that the drag force in their case exceeded the thermal force by at least 1 order of magnitude,
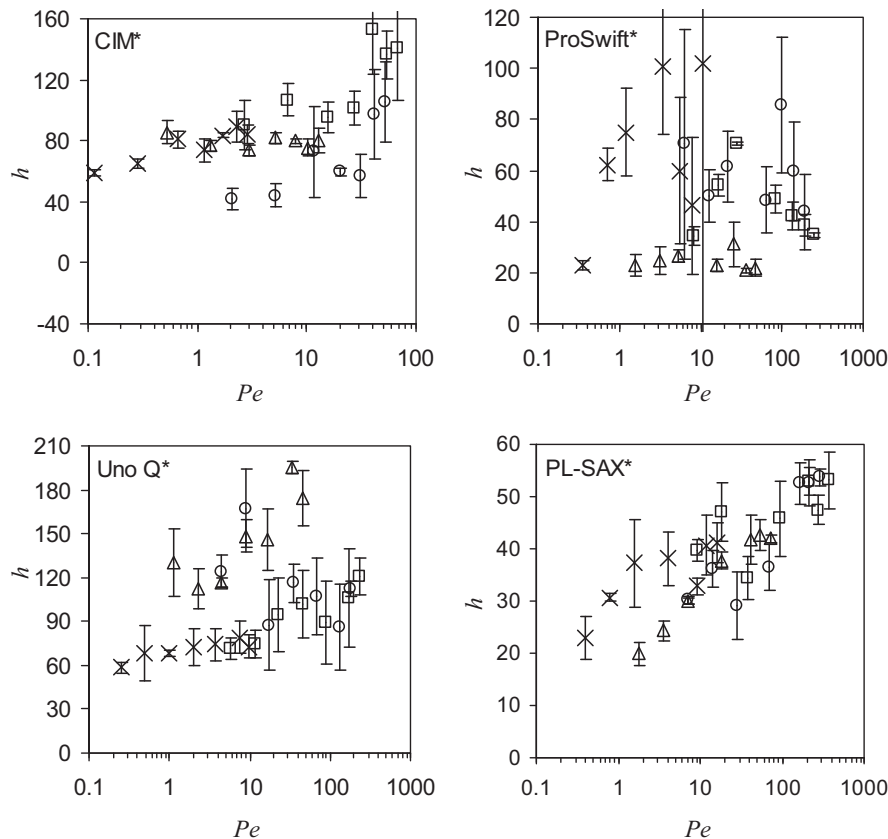

Fig. 8. Reduced plate height as a function of dimensionless flow velocity for non-interacting pulses of NaCl ($\times$), UMP ($\triangle$), ovalbumin ($\bigcirc$), and BSA ($\square$) on the four stationary phases. Data are corrected for temporal distortion. Error bars indicate one standard deviation ($n = 3$).

Table 5
Results of fitting the h data in Fig. 8 (and the corresponding data without correction for temporal distortion) to Eq. (27). A and C are dimensionless. Error estimates indicate 90% confidence intervals. Data in the top part are corrected only for extra-column effects, whereas the data on the bottom (indicated by asterisk) are also corrected for temporal distortion.

	NaCl	UMP	Ovalbumin	BSA	Ad5
A					
CIM	50 ± 9	64 ± 9	-12 ± 44	53 ± 33	157
ProSwift	54 ± 35	21 ± 4	48 ± 2	40 ± 17	157 ± 30
Uno Q	67 ± 6	122 ± 18	126 ± 31	79 ± 11	152 ± 105
PL-SAX	30 ± 6	26 ± 6	28 ± 6	40 ± 6	69 ± 33
C					
CIM	10.3 ± 5.3	-2.1 ± 1.2	1.1 ± 1.5	0.7 ± 0.8	n/a
ProSwift	2.2 ± 6.1	-0.1 ± 0.2	-0.1 ± 0.2	-0.1 ± 0.1	n/a
Uno Q	1.0 ± 1.2	1.6 ± 0.8	-0.2 ± 0.3	0.2 ± 0.1	n/a
PL-SAX	0.7 ± 0.7	0.3 ± 0.2	0.1 ± 0.0	0.0 ± 0.0	n/a
A^*					
CIM	65 ± 9	80 ± 6	41 ± 17	92 ± 20	156
ProSwift	55 ± 33	25 ± 4	63 ± 18	54 ± 14	156 ± 30
Uno Q	66 ± 6	121 ± 17	125 ± 30	80 ± 11	152 ± 105
PL-SAX	30 ± 6	26 ± 6	32 ± 5	41 ± 6	69 ± 33
C^*					
CIM	8.9 ± 5.3	-0.1 ± 0.8	1.2 ± 0.6	0.9 ± 0.5	n/a
ProSwift	2.9 ± 6.0	0.0 ± 0.2	0.0 ± 0.2	-0.1 ± 0.1	n/a
Uno Q	1.1 ± 1.1	1.6 ± 0.8	-0.2 ± 0.3	0.2 ± 0.1	n/a
PL-SAX	0.7 ± 0.7	0.3 ± 0.2	0.1 ± 0.0	0.0 ± 0.0	n/a

suggesting that the elution of cells may have been primarily due to the drag force of the moving liquid and not due to the thermal motion of the cells. For large bioparticles, static binding capacity, expanded bed capacity, and maximum dynamic binding capacity can all differ depending on the drag in each system.

4.3. Band broadening and skew

4.3.1. Non-binding conditions

Minimizing band width is important for improving resolution and minimizing dilution. Since bands can be eluted under non-adsorbing or partially retentive conditions, both cases are considered here. Fig. 8 shows the dependence of h on flow rate under non-adsorbing conditions. The data have large error bars because h is a ratio of moments, which have significant error bars of their own. Additional increases in the size of the error bars resulted from correcting for extra-column dispersion. Data for Ad5 are not included in Fig. 8 because proper peak analysis was not possible, except at very low flow rates, due to virus entrapment [24].

To quantify the data in Fig. 8, h can be broken down into three components using the van Deemter approach [48]:

$$h = A + \frac{B}{Pe} + CPe, \tag{26}$$

where A accounts for convective dispersion, B/Pe represents axial diffusion, and CPe accounts for mass transfer limitations for transport of the analyte to the adsorbent surface and within the adsorbent, where relevant. With the longitudinal diffusion term being negligible at the flow rates studied here, Eq. (26) simplifies

to

$$h = A + CPe. \tag{27}$$

The results of the fitting are shown in Table 5, and indicate that temporal distortion generally had little effect in this case. For Ad5, only the data at the lowest flow rate could be properly analyzed due to convective entrapment of the virus particles at higher flow rates [24], so A in Table 5 for Ad5 is estimated as the h value at the lowest flow rate. The A term was found to be generally dominant, indicating that the dependence of h on flow rate is fairly weak in most cases, so the majority of the band broadening is due to convective dispersion; diffusive limitations are relatively small in materials of this kind. The relative lack of band broadening dependence on flow rate is a well-known benefit of the monolith technology [61–63]. Previous studies in perfusive beds under non-adsorbing conditions have also shown that h increases with analyte size and flow rate, although the increase with flow rate diminishes at high flow rates [3–5,47,64–66]. The data of Frey et al. [4] indicate that h is reduced significantly by an increase in perfusion (larger intrabead pores).

Comparing the stationary phases in Table 5 shows that PL-SAX gave the lowest h. Since small molecules are often used for evaluation of packed beds, it is of interest to compare h for small molecules and biologics on a given stationary phase. The results in Table 5 indicate that, for order-of-magnitude estimates, small molecules predict protein h values reasonably well under non-adsorbing conditions – the differences between values for the two small molecules and between those for the two proteins are comparable to the differences between values for the small molecules

Table 6
Summary of skew results from runs under non-interacting conditions (averaged for all flow rates). Error estimates indicate one standard deviation. Data at the top were corrected only for extra-column effects, neglecting temporal distortion, whereas data on the bottom were corrected for both.

	NaCl	UMP	Ovalbumin	BSA	Ad5
Skew					
CIM	2.7 ± 1.1	2.9 ± 0.6	Imaginary	1.8 ± 3.4	2.1
ProSwift	Imaginary	7.4 ± 0.6	Imaginary	5.6 ± 2.9	2.9
Uno Q	2.7 ± 0.3	3.8 ± 0.3	3.1 ± 0.6	2.9 ± 0.4	1.6
PL-SAX	2.4 ± 0.9	2.5 ± 0.3	1.9 ± 1.8	2.5 ± 0.3	1.7
Skew*					
CIM	2.1 ± 0.7	2.0 ± 0.2	1.7 ± 0.6	2.1 ± 0.4	1.6
ProSwift	6.1 ± 2.1	5.7 ± 0.5	4.3 ± 1.3	3.4 ± 1.1	2.6
Uno Q	2.4 ± 0.4	3.5 ± 0.3	2.6 ± 0.5	2.5 ± 0.4	1.2
PL-SAX	2.1 ± 0.9	2.3 ± 0.3	2.0 ± 0.1	2.0 ± 0.3	1.4

Table 7
Results of fitting the constant J in Eq. (28) to h vs. k' data. Temporal distortion had no significant effect on these results (data shown are not corrected for it). Error estimates indicate 90% confidence interval; u_s = 1 cm/min.

J	UMP	Ovalbumin	BSA
CIM	370 ± 230	3160 ± 1710	3980 ± 860
ProSwift	480 ± 670	6830 ± 5280	6000 ± 5710
Uno Q	−290 ± 80	4510 ± 2430	3590 ± 2850
PL-SAX	30 ± 40	2950 ± 2030	870 ± 370

and the proteins. Plieva et al. showed that, on their monolith, h was approximately the same for small molecules, proteins, and cells [62]. For a conventional packed bed, h has been reported to increase with both flow rate and analyte size [67].

For the runs in Fig. 8, the corresponding skew was generally independent of flow rate. Temporal distortion does not change this trend, but without the correction the *skew* values were higher. Additionally, some *skew* values may be imaginary if the uncorrected second moment of the no-column control happens to be larger than that with the column in place. Taking the average of the skew values at different flow rates allows comparison of different stationary phase-analyte combinations (Table 6). For Ad5, only the data at the lowest flow rate are included in Table 6 because of the entrapment at higher flow rates [24]. The skew for the ProSwift monolith was roughly double that for the other stationary phases, which were similar. Positive skew values indicate that the peaks tailed in all cases, even after correcting for temporal distortion and extra-column effects. The skew magnitudes for these stationary phases (Table 6) are quite large. To put this in perspective: observed asymmetries for normal runs were, on average, 30% higher than the observed skew values and for well-packed conventional beds, asymmetry is typically between around 0.7 and 1.5.

4.3.2. Retentive conditions

In addition to the flow rate, retention can also affect h and skew. The C term in Eq. (27) is constant for unretained solutes, but it depends on the retention factor [68–71]. To account for this dependence explicitly, Eq. (27) can be written in the form [50]

$$h = A + J \frac{k'}{(1 + k')^2}, \tag{28}$$

where J is constant for a given flow rate. Since all experiments under retentive conditions ($k' > 0$) were performed at a constant linear flow rate of 1 cm/min, J was fitted to Eq. (28) by linear regression and the results are summarized in Table 7. Although the fit is somewhat poor, it is clear that the increase in h with k' is far greater for the proteins than for the small molecule on all four stationary phases. Temporal distortion had little effect on these trends.

While band spreading generally increased with retention (at least in the useful range of k'), the skew decreased with increasing k' in most cases [36]. The A term in Eq. (28) (convective dispersion) is assumed not to be affected by retention, but it is possible that, in pores of diameter not much larger than the bioparticles, the flow profile is affected by the binding of the bioparticles. Data for Ad5 are not included in Table 7 because those k' curves were very steep and only one or two valid k' points were obtained (see Fig. 5). The UMP/Uno Q combination is the only outlier from the general trend that $J > 0$.

Although Eq. (28) suggests that the C term is 0 under nonbinding conditions, Table 5 shows that, when $k' = 0$, C is, on average, positive, albeit small. Another potential problem with Eq. (28) is that it predicts that h should decrease with k' at $k' > 1$, which was not observed by Huo et al. [68], nor is it supported by our UMP data. For the proteins, obtaining data at $k' > 1$ on these stationary phases was not practical because, as Fig. 4 shows, the peaks became extremely

smeared and indistinguishable from noise at these mildly retentive conditions. Such dramatic band broadening with increased retention was attributed by Huo et al. to the lack of a stagnant zone in the polymeric monoliths [68]. In contrast, for conventional small-pore resins, the C term is only weakly dependent on retention [68].

5. Conclusions

Larger bioparticles tend to exhibit stronger binding to ion-exchangers and a more abrupt transition from a non-eluting to a non-retentive state with increasing I. To obtain the most concentrated product pool, elution of large macromolecules should be carried out under conditions of minimal retention. Efficient purification of larger biologics, such as viruses, can be attained by loading at higher I, which would minimize binding of smaller contaminants; a small increase in I would then be sufficient for eluting virus particles while minimizing co-elution of stronger-binding contaminants.

For sufficiently large biologics ($\Phi > 1$ in Eq. (19) or (21)) bound to a monolithic bed or on the outside of resin beads, the drag on the bound bioparticles imposed by the moving liquid is predicted to reduce k' and can be the dominant force for desorption during elution, as opposed to the entropic/thermal force, which is the main cause for desorption of small molecules and proteins. Small molecules are reasonable predictors of protein band broadening when the protein is not retained, but underestimate it under retentive conditions.

The simple algorithm developed for estimating temporal distortion and extra-column effects is useful for checking column packing quality and for other applications that involve analyzing pulse injections with fixed-position detectors. The effect of temporal distortion is inversely related to N and, all else being equal, the smaller the bed height, the more skewed a peak would appear to be. Correction for temporal distortion is recommended when accounting for extra-column effects because N is small for the no-column controls. The use of the classic method for peak analysis often results in significant errors, so the MoM is recommended instead, especially since the MoM makes it easier to estimate temporal distortion and extra-column effects. Properly calculated N using the MoM avoids the need for finding As or *skew*, which are sensitive to noise. The plate height should be normalized by permeability to allow comparison among monoliths and beds packed with either spherical beads or other packing materials; it also automatically accounts for compressibility and particle size distribution in packed beds.

Symbols

A	term in van Deemter equation that accounts for convective dispersion; absorbance (absorbance units, AU)
Ad5	human adenovirus type 5
As	asymmetry of a peak at 10% of its height (time between peak maximum and tail/time between peak maximum and the front of the peak), dimensionless
B	term in van Deemter equation that accounts for axial diffusion
B_{ps}	characteristic particle–surface electrostatic energy, dimensionless (scaled by kT)
BSA	bovine serum albumin
C	term in van Deemter equation that accounts for mass transfer limitations
D	diffusivity in free solution (m^2/s)
D_{ax}	axial dispersion coefficient (m^2/s)
d_b	bioparticle diameter (m)

d_e	diameter equivalent to that of a resin bead in a packed bed with the same K value (m)
d_p	pore diameter (m)
d_r	resin bead diameter (m)
F_d	drag force (N)
f	fraction of peak height, dimensionless
H	plate height (m)
h	reduced plate height, dimensionless (scaled by d_e)
I	ionic strength (mol/L)
J	a dimensionless quantity that accounts for the magnitude of change in plate height with changing retention; in van Deemter equation, $J = CPe(1+k')^2/k'$
K	permeability (m^2)
k	Boltzmann constant $= 1.380662 \times 10^{-23}$ J/K
k'	retention factor, dimensionless
L	length of chromatographic bed (m)
MoM	method of moments
m_i	ith moment of a peak (AU s for m_0 and s^i for $m_i > 0$)
m_i'	central moment of a peak; for $i > 0$, it is normalized by the peak area
m_i^*	m_i corrected for temporal distortion
N	number of theoretical plates, dimensionless
n	number of replicates
Pe	$\equiv d_e(u_s/\varepsilon)/D$, Péclet number for convection vs. diffusion in porous media, dimensionless
Pe^*	$\equiv Lu/D_{ax}$, macroscopic Péclet number for quantifying temporal distortion, dimensionless
pI	isoelectric point
T	temperature (K)
t	time (s)
t_R	residence time (s)
u	velocity of the center of mass of a pulse (m/s)
u_s	superficial mobile phase velocity (m/s)
V_0	unretained volume; void volume apparent for a given probe (m^3)
V_R	retained volume (m^3)
w_h	width of a peak at half height (s)
y	normal distance from pore surface, scaled by d_p
Z	dimensionless distance from bed entrance in the axial direction, scaled by L
Z_p	negative of slope of log k' vs. log I plot
ε	total porosity of a chromatographic bed, dimensionless
ε_i	interstitial porosity in a packed bed, dimensionless
μ	viscosity (Pa s)
ρ	concentration of analyte that makes up a chromatographic peak, normalized such that the peak area is 1
ρ_{max}	peak height, normalized such that the peak area is 1
τ	$\equiv tu/L$, dimensionless time (normalized by residence time)
τ_{max}	τ at which peak maximum occurs
Φ	dimensionless ratio of drag force to thermal force for an adsorbed bioparticle in either packed beds or monolithic porous media, including membranes or filters

Additional subscripts

f	quantity at which peak is at a fraction f of its height (usually two values)
S	spatial
T	temporal

Acknowledgements

References

[1] M. Edelstein, J. Gene Med. (2009), http://www.wiley.co.uk/genmed/clinical.
[2] J.K. Raty, J.T. Pikkarainen, T. Wirth, S. Yla-Herttuala, Curr. Mol. Pharmacol. 1 (2008) 13.
[3] N.B. Afeyan, S.P. Fulton, N.F. Gordon, I. Mazsaroff, L. Varady, F.E. Regnier, Nat. Biotechnol. 8 (1990) 203.
[4] D.D. Frey, E. Schweinheim, C. Horvath, Biotechnol. Prog. 9 (1993) 273.
[5] M. McCoy, K. Kalghatgi, F.E. Regnier, N. Afeyan, J. Chromatogr. A 743 (1996) 221.
[6] D. Whitney, M. McCoy, N. Gordon, N. Afeyan, J. Chromatogr. A 807 (1998) 165.
[7] J.L. Liao, R. Zhang, S. Hjerten, J. Chromatogr. 586 (1991) 21.
[8] Y. Liu, V. Antonucci, Y. Shen, A. Vailaya, N.J. Wu, J. Liq. Chromatogr. Relat. Technol. 28 (2005) 341.
[9] J. Urthaler, R. Schlegl, A. Podgornik, A. Strancar, A. Jungbauer, R. Necina, J. Chromatogr. A 1065 (2005) 93.
[10] H.F. Zou, X.D. Huang, M.L. Ye, Q.Z. Luo, J. Chromatogr. A 954 (2002) 5.
[11] B.B. Han, R. Specht, S.R. Wickramasinghe, J.O. Carlson, J. Chromatogr. A 1092 (2005) 114.
[12] R. van Reis, A. Zydney, J. Membr. Sci. 297 (2007) 16.
[13] H.W. Yang, C. Viera, J. Fischer, M.R. Etzel, Ind. Eng. Chem. Res. 41 (2002) 1597.
[14] P. Gagnon, R. Richieri, 2nd Wilbio Conference on Purification of Biological Products, Thousand Oaks, California, 2006.
[15] G. Iberer, R. Hahn, A. Jungbauer, LCGC North Am. 17 (1999) 998.
[16] A.E. Rodrigues, V.G. Mata, M. Zabka, L. Pais, in: F. Švec, T.B. Tennikova, Z. Deyl (Eds.), Monolithic Materials: Preparation, Properties, and Applications, Elsevier, Boston, 2003, p. 333.
[17] E.I. Trilisky, H. Koku, K.J. Czymmek, A.M. Lenhoff, J. Chromatogr. A 1216 (2009) 6365.
[18] D.A. Hammer, S.M. Apte, Biophys. J. 63 (1992) 35.
[19] M.B. Lawrence, C.W. Smith, S.G. Eskin, L.V. Mcintire, Blood 75 (1990) 227.
[20] D. Pappas, K. Wang, Anal. Chim. Acta 601 (2007) 26.
[21] H. Bittiger, in: H. Bittiger, H.P. Schnebli (Eds.), Concanavalin A as a Tool, Wiley, London, 1976, p. 435.
[22] S.K. Sharma, P.P. Mahendroo, J. Chromatogr. 184 (1980) 471.
[23] R. Vennapusa, S.M. Hunegnaw, R.B. Cabrera, M. Fernandez-Lahore, J. Chromatogr. A 1181 (2008) 9.
[24] E.I. Trilisky, A.M. Lenhoff, Biotechnol. Bioeng. 104 (2009) 127.
[25] K.J. Fountain, U.D. Neue, E.S. Grumbach, D.M. Diehl, J. Chromatogr. A 1216 (2009) 5979.
[26] S.-C. Pai, J. Chromatogr. A 950 (2002) 271.
[27] J.Å. Jönsson, J. Chromatogr. 150 (1978) 11.
[28] E.N. Lightfoot, J.L. Coffman, F. Lode, Q.S. Yuan, T.W. Perkins, T.W. Root, J. Chromatogr. A 760 (1997) 139.
[29] D.K. Roper, E.N. Lightfoot, J. Chromatogr. A 702 (1995) 3.
[30] J.Å. Jönsson, Chromatographic Theory and Basic Principles, Dekker, New York, 1987.
[31] B.A. Bidlingmeyer, F.V. Warren Jr., Anal. Chem. 56 (1984) 1583A.
[32] G. Guiochon, D.G. Shirazi, A. Felinger, A.M. Katti, Fundamentals of Preparative and Nonlinear Chromatography, 2nd ed., 2006.
[33] A.M. Lenhoff, J. Chromatogr. 384 (1987) 285.
[34] G.I. Taylor, Proceedings of the Royal Society of London. Series A, Mathematical and Physical Sciences 219 (1953) 186.
[35] E. Grushka, J. Phys. Chem. 76 (1972) 2586.
[36] E.I. Trilisky, Stationary and mobile phase selection for ion-exchange chromatography of viruses, PhD Thesis, Dept Chem Eng, University of Delaware (2009).
[37] A. Shankar, A.M. Lenhoff, AIChE 35 (1989) 2048.
[38] D.J. Acheson, Elementary Fluid Dynamics, Oxford University Press, 1990.
[39] P. DePhillips, A.M. Lenhoff, J. Chromatogr. A 883 (2000) 39.
[40] A.J. Matheson, J. Phys. C: Solid State 7 (1974) 2569.
[41] E.I. Trilisky, A.M. Lenhoff, J. Chromatogr. A 1142 (2007) 2.
[42] E.R. Nightingale, J. Phys. Chem. 63 (1959) 1381.
[43] S. Miller, J. Janin, A.M. Lesk, C. Chothia, J. Mol. Biol. 196 (1987) 641.
[44] J.J. Rux, R.M. Burnett, in: P. Seth (Ed.), Adenoviruses: Basic Biology to Gene Therapy, 1999.
[45] R.A. Shalliker, H.J. Catchpoole, G.R. Dennis, G. Guiochon, J. Chromatogr. A 1142 (2007) 48.
[46] B.G. Huyghe, X.D. Liu, S. Sutjipto, B.J. Sugarman, M.T. Horn, H.M. Shepard, C.J. Scandella, P. Shabram, Hum. Gene Ther. 6 (1995) 1403.
[47] A.L. Geng, K.C. Loh, J. Chromatogr. A 918 (2001) 37.
[48] J.J. van Deemter, F.J. Zuiderweg, A. Klinkenberg, Chem. Eng. Sci. 5 (1956) 271.
[49] F.C. Leinweber, D. Lubda, K. Cabrera, U. Tallarek, Anal. Chem. 74 (2002) 2470.
[50] R. Hahn, A. Jungbauer, Anal. Chem. 72 (2000) 4853.
[51] A. Podgornik, M. Barut, S. Jaksa, J. Jancar, A. Strancar, J. Liq. Chromatogr. Relat. Technol. 25 (2002) 3099.
[52] A. Velayudhan, C. Horvath, J. Chromatogr. 367 (1986) 160.
[53] W.C. Chew, P.N. Sen, J. Chem. Phys. 77 (1982) 2042.
[54] M.R. Oberholzer, J.M. Stankovich, S.L. Carnie, D.Y.C. Chan, A.M. Lenhoff, J. Colloid Interf. Sci. 194 (1997) 138.
[55] J.S. Rowlinson, Physica A 156 (1989) 15.
[56] J.E. Sader, J. Colloid Interf. Sci. 188 (1997) 508.
[57] Y. Yuan, M.R. Oberholzer, A.M. Lenhoff, Colloid Surf. A 165 (2000) 125.
[58] P. DePhillips, A.M. Lenhoff, J. Chromatogr. A 933 (2001) 57.

[59] S.R. Dziennik, E.B. Belcher, G.A. Barker, M.J. DeBergalis, S.E. Fernandez, A.M. Lenhoff, PNAS 100 (2003) 420.
[60] P. Arvidsson, F.M. Plieva, I.N. Savina, V.I. Lozinsky, S. Fexby, L. Bulow, I.Y. Galaev, B. Mattiasson, J. Chromatogr. A 977 (2002) 27.
[61] A. Jungbauer, R. Hahn, J. Sep. Sci. 27 (2004) 767.
[62] F.M. Plieva, I.N. Savina, S. Deraz, J. Andersson, I.Y. Galaev, B. Mattiasson, J. Chromatogr. B 807 (2004) 129.
[63] S. Vogt, R. Freitag, Biotechnol. Progr. 14 (1998) 742.
[64] G. Carta, M.E. Gregory, D.J. Kirwan, H.A. Massaldi, Sep. Technol. 2 (1992) 62.

[65] S. Katoh, M. Terashima, E. Sada, H. Utsumi, Y. Kamiya, K. Yamada, T. Majima, J. Ferment. Bioeng. 78 (1994) 246.
[66] N.B. Afeyan, N.F. Gordon, I. Mazsaroff, L. Varady, S.P. Fulton, Y.B. Yang, F.E. Regnier, J. Chromatogr. 519 (1990) 1.
[67] S. Yamamoto, E. Miyagawa, J. Chromatogr. A 852 (1999) 25.
[68] Y. Huo, P.J. Schoenmakers, W.T. Kok, J. Chromatogr. A 1175 (2007) 81.
[69] J.H. Knox, H.P. Scott, J. Chromatogr. 282 (1983) 297.
[70] H. Poppe, R. Stol, W.T. Kok, J. Chromatogr. A 965 (2002) 75.
[71] A.-M. Siouffi, J. Chromatogr. A 1126 (2006) 86.